Noise Analysis of a New Singularity Index

Gautam S. Muralidhar, *Member, IEEE*, Alan C. Bovik, *Fellow, IEEE*, and Mia K. Markey, *Senior Member, IEEE*

***Abstract*—We analyze the noise sensitivity of a new singularity index that was designed to detect impulse singularities in signals of arbitrary dimensionality while rejecting step-like singularities see Muralidhar *et al.*, *IEEE Signal Process. Lett.*, vol. 20, no. 1, pp. 7–10, 2013 and Muralidhar *et al.*, *Proc. IEEE Int. Conf. Image Process.*, 2012. For example, the index responds strongly to curvilinear masses (ridges) in images, while weakly to jump discontinuities (edges). We analyze the detection power of the index in the presence of noise. Our analysis is geared towards answering the following questions: a) in the presence of noise only, what is the probability of falsely detecting an impulse given a threshold; b) given an impulse submerged in noise, what is the probability of detecting it given a threshold; and c) since the index is designed to be edge suppressing, what is the probability of incorrectly detecting an edge submerged in noise given a threshold. We compare the detection power of the index with that of a nominal impulse detector, the second derivative operator. Simulations and example applications in 1-D and 2-D reveal the efficacy of the new singularity index for correctly detecting impulses submerged in noise, while suppressing edges. A software version of the 2-D singularity index can be downloaded from: http://live.ece.utexas.edu/research/SingularityIndex/SingularityIndexCode.zip.**

***Index Terms*—Edges, impulses, singularities, singularity detection, statistical analysis.**

I. Introduction

SINGULARITY detection has been a widely studied problem in signal and image processing. For example, detecting transients or peaks in 1-D signals such as mass spectrometry signals obtained from biological fluids such as serum is important in proteomic pattern diagnosis, e.g., [3], [4]. In images, singularities often manifest as isolated impulse or curvilinear masses, which are commonly referred to as ridges, and step discontinuities, which are commonly referred to as edges [5]–[10]. Reliable detection of curvilinear masses in images is important in many applications such as the detection of blood vessels and cancers in medical images, filaments in images of biological specimens, and roads and river deltas in satellite images [10].

We recently designed a new index to detect impulse singularities in signals of arbitrary dimensionality [1], [2]. It is defined as the dimensionless ratio

$$(\psi f)(t) = \frac{|f(t)f''(t)|}{C + |f'(t)|^2}, \tag{1}$$

where $f(t), t \in R$ is a 1-D signal, $f'(t)$ and $f''(t)$ are the first and second derivatives of $f(t)$, respectively, and the constant $C \in R$. As explained in [1], we assume the nominal value $C = 1$. Hence

$$(\psi f)(t) = \frac{|f(t)f''(t)|}{1 + |f'(t)|^2}. \tag{2}$$

The singularity index (2) is closely related to an energy operator developed by Teager and Kaiser [11], which has been employed for demodulating AM-FM signals [12]. The index (2) responds strongly to impulse masses whose twice derivative is large and once-derivative is small. To see this, model a smoothed 1-D impulse (a smoothed Dirac) as a gaussian of height $K > 0$ and scale w: $f(t) = K\delta_w(t) = Ke^{\frac{-t^2}{2w^2}}$. Then at $t = 0$, $(\psi f)(0) = \left|\frac{K^2}{w^2}\right|$. Hence, the index response at the origin increases monotonically as either K increases or w decreases. The index is not sensitive to the polarity of the impulse, but is easily modified to reflect signal polarity. However, it is sensitive to the signal level (bias).

Since many applications require bias-free impulse detection, the index response can be easily debiased by subtracting a low-pass version of the signal prior to applying the index. As detailed in [1], a principled way to accomplish this uses a gaussian low-pass debiasing filter $g_\lambda(t) = \frac{1}{\sqrt{2\pi}\lambda}e^{\frac{-t^2}{2\lambda^2}}$, where $\lambda \geq w\sqrt{\frac{1-\epsilon^2}{\epsilon^2}}$. This choice of the filter space constant ensures that the response to a gaussian impulse will be reduced by no more than a fraction ϵ.

On the other hand, edges whose once derivative is large and twice derivative is small produce minimal responses to the index. Model a 1-D edge profile as a Heaviside step $u(t)$ of height $K > 0$ smoothed by a gaussian $g_w(t)$: $f(t) = K\Phi\left(\frac{t}{w}\right)$, where $\Phi\left(\frac{t}{w}\right) = \frac{1}{\sqrt{2\pi}}\int_{-\infty}^{\frac{t}{w}} e^{\frac{-x^2}{2}}dx$. Then the index response vanishes at the origin: $(\psi f)(0) = 0$.

The singularity index in (2) operates directly on the signal. This is not practical in real applications since derivative computations are not stable in the presence of noise. Hence, define the smoothed singularity index

$$(\psi_\sigma f)(t) = \frac{|g_\sigma * f(t)|\,|g''_\sigma * f(t)|}{1 + |g'_\sigma * f(t)|^2}, \tag{3}$$

Manuscript received December 04, 2012; revised June 03, 2013 and September 06, 2013; accepted September 14, 2013. Date of publication September 25, 2013; date of current version November 12, 2013. The associate editor coordinating the review of this manuscript and approving it for publication was Prof. Andrea Cavallaro. This work was supported under NSF grant number IIS-1116656.

G. S. Muralidhar was with the Department of Biomedical Engineering, The University of Texas at Austin, TX 78712 USA. He is now with VuCOMP, Inc., Plano, TX 75024 USA (e-mail: gautam.sm@utexas.edu)

M. K. Markey is with the Department of Biomedical Engineering, The University of Texas at Austin, TX 78712 USA.

A. C. Bovik is with the Department of Electrical and Computer Engineering, The University of Texas at Austin, TX 78712 USA.

Color versions of one or more of the figures in this paper are available online at http://ieeexplore.ieee.org.

Digital Object Identifier 10.1109/TSP.2013.2283460

1053-587X © 2013 IEEE

where $(\psi_\sigma f)(t)$ is the shorthand notation for $(\psi f)(t,\sigma)$ used in [1] and g_σ is a unit-area gaussian:

$$g_\sigma(t) = \frac{1}{\sqrt{2\pi}\sigma} e^{\frac{-t^2}{2\sigma^2}}. \tag{4}$$

The smoothed singularity index is regularized similar to the regularized Teager energy operator discussed in [13], [14].

The smoothing filter serves two objectives. First, it stabilizes (regularizes) the derivative computations in the presence of noise, and second, it provides a framework for multi-scale (scale-space) representation of the signal. As shown in [1], for a smoothed gaussian impulse of height $K > 0$ and width w, the scale-normalized singularity index

$$(\psi_{\sigma,norm} f)(t) = \sigma^{2\gamma}(\psi_\sigma f)(t), \tag{5}$$

where $\gamma \in R$ attains a scale-space peak response at the origin when $\sigma = \sqrt{\frac{2\gamma}{4-2\gamma}}w$, which matches the smoothed impulse scale when $\gamma = 1$. Substituting $\gamma = 1$ and $\sigma = w$ in (5) yields a scale-space peak response of $(\psi_{\sigma=w,norm} f)(0) = \frac{K^2}{4}$, which is scale invariant in the absence of noise [1]. Note that the scale-normalized singularity index is based on Lindeberg's scale selection methodology that involves finding the local extrema over scales of γ-normalized derivatives [8].

Here, we shall analyze the impulse detection power of the smoothed 1-D singularity index in the presence of noise. These analyses are important since they reveal how predictable the index is when applied to an impulse that is submerged in noise. The remainder of the paper is organized as follows: in Section I-A, we provide a brief review of the prior work on singularity detection and place the new singularity index in context. In Section II, we establish the existence of the low-order moments (mean and variance) of the response of ψ_σ to zero-mean, wide sense stationary (WSS) Gaussian random noise. In Section III, we conduct a false alarm analysis, finding the probability of false impulse detection in the presence of noise only followed by an analysis of the probability of true impulse detection for an impulse submerged in noise. Further, since the index is designed to be edge suppressing, we also study the probability of incorrectly detecting an edge submerged in noise in Section IV. In Section V, we use the results of our analyses to extract peak locations from example 1-D mass spectrometry signals. Then we also use the results of our analyses as a guide to determine thresholds for extracting curvilinear structures from example 2-D images afflicted with noise in Section VI. In Section VII, we demonstrate the potential of the new singularity index for automatic segmentation of vessels on retina images as an example 2-D application. Finally, we conclude the paper in Section VIII.

A. Review of Singularity Detection

Mallat and Hwang [6] and Mallat and Zhong [15] studied singularity detection in the context of wavelet theory. They showed that the singularities in a signal can be detected and characterized by the local modulus maxima of the multi-scale wavelet transform of the signal. The Lipschitz exponent estimated from the evolution of the wavelet transform modulus maxima across scales is used to reveal whether the signal varied smoothly, or whether there was an edge, or an impulse singularity [6], [15]. As in the current study, the Dirac function and the smoothed Dirac function (a gaussian pulse) are used to model impulse singularities. They also cast Canny's multi-scale edge detector in the wavelet analysis framework [15]. The wavelet considered in their analyses is the simple first derivative of a gaussian smoothing function [15].

Lindeberg studied ridge detection in a scale-space framework [7], [8]. He proposed ridge strength measures based on the Eigen values of the Hessian matrix of the gaussian smoothed image. Multi-scale analysis was achieved by varying the scale of the smoothing gaussian function. One of Lindeberg's ridge strength measures is the maximum absolute Eigen value of the Hessian matrix computed at each image location, which corresponds to the maximum absolute value of the directional second derivative. Similar to Canny's edge detector, Lindeberg's ridge detector can be cast within the wavelet framework [15], with the wavelet being the second derivative of a gaussian function.

The new singularity index (3) is designed to detect impulse (ridge) singularities. A similarity between Mallat's [15] and Lindeberg's analysis [7], [8] is that their impulse (ridge) measures are based on first and second derivatives of the signal. By comparison, the new singularity index is a non-linear combination of the signal, its first and second derivatives. Throughout this paper, we compare the performance of the new singularity index with the second derivative operator, which is one of the measures put forth by Lindeberg for detection of ridges in images [7], [8].

Finally, note that several non linear filters based on order statistics have been proposed for impulse detection (e.g., [16]). However, these filters are typically used to remove impulse noise (salt and pepper noise) in images. While they are known to work well on impulse noise, their extensions to detect sustained multi-scale curvilinear structures such as ridges in images is not straight forward and often involves ad-hoc combinations of many filters and several post-processing steps.

II. Low-Order Moments of ψ_σ

We begin by establishing the existence of the low-order moments (mean and the variance) of the smoothed singularity index when applied to a random signal $n(t)$. These moments reveal useful insights into the stability and the predictability of the index when applied to signals submerged in noise.

Assume that $n(t)$ is a zero-mean WSS gaussian random process with auto-correlation function

$$R_n(\tau) = q^2\delta(\tau), \tag{6}$$

where the input noise variance is $R_n(0) = q^2$. The assumption of wide sense stationarity and gaussianity allows for a tractable statistical analyses of ψ_σ. We will deal with the slightly more complex non-zero mean case when we study the statistical behavior of the index when applied to a deterministic signal immersed in a random zero-mean noise process.

Let $n_\sigma(t) = n(t) * g_\sigma(t)$, $n'_\sigma(t) = (n(t) * g_\sigma(t))'$, and $n''_\sigma(t) = (n(t) * g_\sigma(t))''$, where $g_\sigma(t)$ is a unit-area gaussian smoothing filter as defined in (4). All of the processes $n_\sigma(t)$,

$n'_\sigma(t)$ and $n''_\sigma(t)$ are also zero-mean WSS gaussian [17]. Moreover, $n'_\sigma(t)$ is statistically independent of both $n_\sigma(t)$ and $n''_\sigma(t)$. Hence, the singularity index

$$(\psi_\sigma n)(t) = \frac{|n_\sigma(t)||n''_\sigma(t)|}{1+|n'_\sigma(t)|^2} \tag{7}$$

is the ratio of two statistically independent random processes.

Denote the numerator random process in (7) by X and the denominator random process by Y. From Theorem 2 in [18], the ratio X/Y has all the moments up to order $\leq q$ provided the following condition is satisfied:

$$Pr\{|Y| < T\} \leq AT^{\frac{pq}{p-q}(1+\alpha)}, \tag{8}$$

for any α, $A > 0$, integers $p > q$, and $\forall\ 0 < T < \alpha$. Letting $\alpha = 1$, this condition holds since

$$Pr\{|Y| < T\} = Pr\left\{|1+|n'_\sigma|^2| < T\right\} = 0 \leq AT^{\frac{pq}{p-q}(1+\alpha)} \tag{9}$$

$\forall\ A > 0, p > q, 0 < T < 1$, since $1+|n'_\sigma|^2 \geq 1$. We next derive approximations for the mean and the variance of $(\psi_\sigma n)(t)$.

The auto-correlation function of the process $n_\sigma(t)$ is $R_{n_\sigma}(\tau) = g_\sigma(\tau) * g_\sigma(-\tau) * R_n(\tau)$, since $n(t)$ is WSS [17]. This evaluates to

$$R_{n_\sigma}(\tau) = \frac{q^2}{2\sqrt{\pi}\sigma} e^{-\frac{\tau^2}{4\sigma^2}}. \tag{10}$$

Hence, the variance of $n_\sigma(t)$ is

$$var\left[n_\sigma(t)\right] = R_{n_\sigma}(0) = \nu_0^2 = \frac{q^2}{2\sqrt{\pi}\sigma}. \tag{11}$$

Further, the variances of the derivative processes $n'_\sigma(t)$ and $n''_\sigma(t)$ can be written as [17]

$$var\left[n'_\sigma(t)\right] = R_{n'_\sigma}(0) = -R^{(2)}_{n_\sigma}(0) = \nu_1^2 = \frac{q^2}{4\sqrt{\pi}\sigma^3}, \tag{12}$$

and

$$var\left[n''_\sigma(t)\right] = R_{n'_\sigma}(0) = R^{(4)}_{n_\sigma}(0) = \nu_2^2 = \frac{3q^2}{8\sqrt{\pi}\sigma^5}, \tag{13}$$

where $R^{(k)}_{n_\sigma}(\tau) = \frac{d^k R_{n_\sigma}(\tau)}{d\tau^k}$.

In general, it is difficult to derive exact expressions for the statistical mean and variance of (7). However, it is possible to re-write (7) as

$$(\psi_\sigma n)(t) = \left|\frac{n_\sigma(t)n''_\sigma(t)}{1+|n'_\sigma(t)|^2}\right|, \tag{14}$$

since $1+|n'_\sigma(t)|^2$ is positive. Further, let

$$(\psi_\sigma n)(t) = \left|(\hat{\psi_\sigma n})(t)\right|, \tag{15}$$

where $(\hat{\psi_\sigma n})(t) = \frac{n_\sigma(t)n''_\sigma(t)}{1+|n'_\sigma(t)|^2}$. The approximate mean and variance of the ratio $(\hat{\psi_\sigma n})(t)$ can be found using the Taylor expansion [17]:

$$E\left[\frac{X}{Y}\right] = \frac{E[X]}{E[Y]} - \frac{cov[X,Y]}{[E[Y]]^2} + \frac{var[Y]E[X]}{[E[Y]]^3}, \tag{16}$$

and

$$var\left[\frac{X}{Y}\right] = \frac{var[X]}{[E[Y]]^2} - 2\frac{cov[X,Y]E[X]}{[E[Y]]^3} + \frac{var[Y]\,[E[X]]^2}{[E[Y]]^4}, \tag{17}$$

where X and Y are defined as above and $E[\ .\ ]$ denotes expectation.

It can be shown that [12]

$$E[X] = E\left[n_\sigma(t)n''_\sigma(t)\right] = R^{(2)}_{n_\sigma}[0] = -\nu_1^2, \tag{18}$$

$$E[Y] = E\left[1+(n'_\sigma(t))^2\right] = 1 + R_{n'_\sigma}(0) = 1 - R^{(2)}_{n_\sigma}(0) = 1+\nu_1^2. \tag{19}$$

Using Isserlis's formula for the product moment coefficient of normally distributed random variables [19], the variance of the numerator random process evaluates to

$$var[X] = var\left[n_\sigma(t)n''_\sigma(t)\right] = R_{n_\sigma}(0)R^{(4)}_{n_\sigma}(0) + \left[R^{(2)}_{n_\sigma}(0)\right]^2 = \nu_0^2\nu_2^2 + \nu_1^4. \tag{20}$$

The variance of the denominator random process is [17]

$$var[Y] = var\left[1+|n'_\sigma(t)|^2\right] = var\left[[n'_\sigma(t)]^2\right] = 2\left[R^{(2)}_{n_\sigma}(0)\right]^2 = 2\nu_1^4. \tag{21}$$

Substituting (18), (19), (20), (21), and $cov[X,Y] = 0$ (since X and Y are statistically independent) in (16) and (17) yields

$$E\left[(\hat{\psi_\sigma n})(t)\right] = \frac{-\nu_1^2}{1+\nu_1^2} + 2\left(\frac{-\nu_1^2}{1+\nu_1^2}\right)^3. \tag{22}$$

and

$$var\left[(\hat{\psi_\sigma n})(t)\right] = \frac{\nu_0^2\nu_2^2+\nu_1^4}{(1+\nu_1^2)^2} + \frac{2\nu_1^8}{(1+\nu_1^2)^4}. \tag{23}$$

The mean and variance of $(\hat{\psi_\sigma n})(t)$ place bounds on the moments of the singularity index $(\psi_\sigma n)(t)$ as a consequence of Jensen's inequality: $E[(\psi_\sigma n)(t)] > E[(\hat{\psi_\sigma n})(t)]$ and $var[(\psi_\sigma n)(t)] < var[(\hat{\psi_\sigma n})(t)]$.

Finally, Fig. 1 illustrates the mean (top) and variance (bottom) of $(\hat{\psi_\sigma n})(t)$ computed using the Taylor approximation for different values of the input noise variance q^2 as a function of the smoothing filter scale σ. To ascertain the veracity of the Taylor approximation, we plot the mean and variance of $(\hat{\psi_\sigma n})(t)$ computed empirically for simulated zero-mean white gaussian noise at the same values of q^2 and σ. As evident from Fig. 1, the mean and variance of $(\hat{\psi_\sigma n})(t)$ estimated using the Taylor approximation and empirical simulation are nearly identical. It is also evident from Fig. 1 that for each input noise variance, the mean of $(\hat{\psi_\sigma n})(t)$ approaches zero as the smoothing filter scale increases, while the variance of $(\hat{\psi_\sigma n})(t)$ decreases as the smoothing filter scale increases. These properties are desirable since it suggests that as the noise is reduced by increased smoothing, the expected value and the variance of the index response tend towards zero.

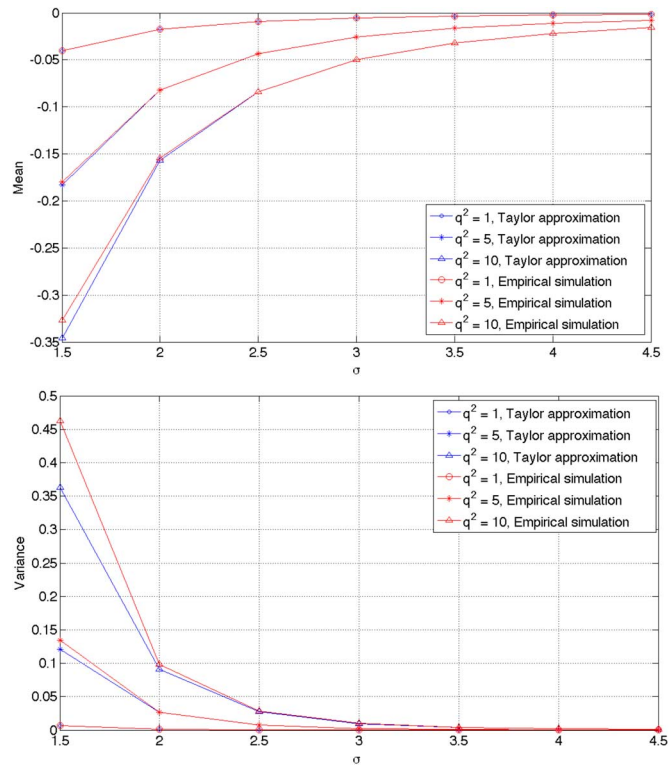

Fig. 1. Mean (top) and variance (bottom) of $\hat{\psi_\sigma}[n(t)]$ estimated using the Taylor approximation (blue) and empirical simulations (red) for different values of the input noise variance q^2 as a function of the smoothing filter scale σ.

III. False Alarm and True Impulse Detection Probabilities

A. False Alarm Probability

Here, we find the probability of false impulse detection given a threshold, when the scale-normalized smoothed singularity index (5) ($\gamma = 1$) is applied to a zero-mean WSS gaussian random process $n(t)$. This is a simple test of whether an impulse singularity will be detected when none is present (false alarm). We only deal with the scale-normalized case, since in real applications the scale-normalized index is most useful for detecting impulses and for obtaining an estimate of their scale/width. Lindeberg [8] first presented scale-normalization in the context of ridge detection and stated that it was necessary to normalize the derivatives computed at each scale of the smoothing gaussian in order to compare the derivative magnitudes across scales and to obtain an estimate of the width of the ridge. We begin by first finding the false alarm probability for the smoothed singularity index and subsequently use this result to find the false alarm probability for the scale-normalized index (5).

As discussed earlier, the random process $(\psi_\sigma n)$ (7) is the ratio of two statistically independent random processes $X = |n_\sigma||n''_\sigma|$ and $Y = 1 + |n'_\sigma|^2$, i.e. $(\psi_\sigma n) = X/Y$. Since n'_σ is a zero-mean gaussian random process, the probability density function (PDF) of Y is given by [17]

$$f_Y(y) = \frac{1}{\sqrt{2\pi(y-1)}\nu_1} exp\left(-\frac{(y-1)}{2\nu_1^2}\right),\ y > 1. \quad (24)$$

The numerator random process is of the form $X = |\hat{X}|$, where $\hat{X} = n_\sigma n''_\sigma$. Since both n_σ and n''_σ are correlated zero-mean gaussian random processes with correlation coefficient $\rho = \frac{-\nu_1^2}{\nu_0\nu_2}$, their product $\hat{X}$ has a PDF that is given by [12]

$$f_{\hat{X}}(x) = \frac{1}{\pi\sqrt{\nu_0^2\nu_2^2 - \nu_1^4}} exp\left(\frac{-x\nu_1^2}{\nu_0^2\nu_2^2 - \nu_1^4}\right) K_0\left(\frac{|x|\nu_0\nu_2}{\nu_0^2\nu_2^2 - \nu_1^4}\right), \quad (25)$$

where $K_0(\,.\,)$ is the modified Bessel function of the second kind and order zero. The PDF of $X = |\hat{X}|$ is given by

$$f_X(x) = f_{\hat{X}}(x) + f_{\hat{X}}(-x),\ x > 0. \quad (26)$$

Hence,

$$f_X(x) = \frac{1}{\pi\sqrt{\nu_0^2\nu_2^2 - \nu_1^4}} K_0\left(\frac{|x|\nu_0\nu_2}{\nu_0^2\nu_2^2 - \nu_1^4}\right) \cdot \left\{exp\left(\frac{-x\nu_1^2}{\nu_0^2\nu_2^2 - \nu_1^4}\right) + exp\left(\frac{x\nu_1^2}{\nu_0^2\nu_2^2 - \nu_1^4}\right)\right\},\ x > 0. \quad (27)$$

Determining a closed form expression for the PDF of $(\psi_\sigma n)$ is generally difficult. However, numerical evaluation of the probabilities involving $(\psi_\sigma n)$ is feasible. Specifically, evaluate the probability

$$Pr\{(\psi_\sigma n) > \tau\} = Pr\{X/Y > \tau\}, \quad (28)$$

where $\tau > 0$ is a threshold. The probability in (28) can be determined as [17]

$$Pr\{X/Y > \tau\} = \int_{x=0}^{\infty}\int_{y=0}^{\frac{x}{\tau}} f_{XY}(x,y)\,\mathrm{d}y\,\mathrm{d}x + \int_{x=-\infty}^{0}\int_{y=\frac{x}{\tau}}^{0} f_{XY}(x,y)\,\mathrm{d}y\,\mathrm{d}x. \quad (29)$$

Since X and Y are statistically independent of each other, (29) becomes

$$Pr\{X/Y > \tau\} = \int_{x=0}^{\infty}\left(\int_{y=0}^{\frac{x}{\tau}} f_Y(y)\,\mathrm{d}y\right) f_X(x)\,\mathrm{d}x + \int_{x=-\infty}^{0}\left(\int_{y=\frac{x}{\tau}}^{0} f_Y(y)\,\mathrm{d}y\right) f_X(x)\,\mathrm{d}x. \quad (30)$$

The second double integral in (30) evaluates to 0 since $f_Y(y) = 0\ \forall\ y \leq 1$. Hence, (30) can be written

$$Pr\{X/Y > \tau\} = \int_{x=0}^{\infty}\left(\int_{y=1}^{\frac{x}{\tau}} f_Y(y)\,\mathrm{d}y\right) f_X(x)\,\mathrm{d}x. \quad (31)$$

Consider the inner integral

$$\int_{y=1}^{\frac{x}{\tau}} f_Y(y)\,\mathrm{d}y = \int_{y=1}^{\frac{x}{\tau}} \frac{1}{\sqrt{2\pi(y-1)}\nu_1} exp\left(-\frac{(y-1)}{2\nu_1^2}\right)\,\mathrm{d}y. \quad (32)$$

On introducing the change of variable $z = y - 1$ and using (3.361) in [20], (32) evaluates to

$$erf\left(\sqrt{\frac{1}{2\nu_1^2}\left(\frac{x}{\tau}-1\right)}\right),\ x \geq \tau, \tag{33}$$

where $erf(\zeta) = \frac{2}{\sqrt{\pi}}\int_0^{\zeta} e^{-t^2}\mathrm{d}t$ is the error function.

Substituting (27) and (33) into (31) yields

$$\begin{aligned} Pr\{X/Y > \tau\} = &\int_{x=\tau}^{\infty} erf\left(\sqrt{\frac{1}{2\nu_1^2}\left(\frac{x}{\tau}-1\right)}\right) \\ &\times \frac{1}{\pi\sqrt{\nu_0^2\nu_2^2-\nu_1^4}}K_0\left(\frac{|x|\nu_0\nu_2}{\nu_0^2\nu_2^2-\nu_1^4}\right) \\ &\times\left\{exp\left(\frac{-x\nu_1^2}{\nu_0^2\nu_2^2-\nu_1^4}\right)\right. \\ &\left.+exp\left(\frac{x\nu_1^2}{\nu_0^2\nu_2^2-\nu_1^4}\right)\right\}\mathrm{d}x. \end{aligned} \tag{34}$$

Making a number of changes of variables in (34) yields

$$\begin{aligned} Pr\left\{(\psi_\sigma n) > \tau\right\} = Pr\{X/Y > \tau\} = &\frac{\sqrt{2}\tau}{\pi}\int_{a=0}^{\infty} erf(\sqrt{a}) \\ &.K_0\left(\left|\sqrt{3}a\tau + \frac{2\sqrt{3\pi}\sigma^3\tau}{q^2}\right|\right) \\ &.\left\{exp\left(-a\tau - \frac{2\sqrt{\pi}\sigma^3\tau}{q^2}\right)\right. \\ &\left.+exp\left(a\tau + \frac{2\sqrt{\pi}\sigma^3\tau}{q^2}\right)\right\}\mathrm{d}a. \end{aligned} \tag{35}$$

Then, it is easily shown that the probability of false impulse detection in noise using the scale-normalized smoothed singularity index $(\psi_{\sigma,norm}n) = \sigma^2(\psi_\sigma n)$ is

$$\begin{aligned} &Pr\left\{(\psi_{\sigma,norm}n) > \tau\right\} \\ &= \frac{\sqrt{2}}{\pi}\frac{\tau}{\sigma^2}\int_{a=0}^{\infty} erf(\sqrt{a}).K_0\left(\left|\frac{\sqrt{3}a\tau}{\sigma^2} + \frac{2\sqrt{3\pi}\tau\sigma}{q^2}\right|\right) \\ &.\left\{exp\left(-\frac{a\tau}{\sigma^2} - \frac{2\sqrt{\pi}\tau\sigma}{q^2}\right)\right. \\ &\left.+exp\left(\frac{a\tau}{\sigma^2} + \frac{2\sqrt{\pi}\tau\sigma}{q^2}\right)\right\}\mathrm{d}a. \end{aligned} \tag{36}$$

We also compare the false alarm rates of the singularity index with the scale-normalized smoothed second derivative operator

$$(\Theta_{\sigma,norm}f)(t) = \sigma^{1.5}(\Theta_\sigma f)(t), \tag{37}$$

where

$$(\Theta_\sigma f)(t) = \left|(f(t) * g_\sigma(t))''\right|. \tag{38}$$

The operator Θ_σ is the simplest nominal impulse detector, which responds strongly to impulses. It produces a minimal response to the center of an edge, but a large response in the edge neighborhood as discussed in [1]. Normalization by $\sigma^{1.5}$ ensures that the maximizing scale matches the impulse scale. Note that the scale normalized second derivative index $(\Theta_{\sigma,norm})$ is precisely equivalent to Lindeberg's *scale-normalized maximum eigenvalue of the Hessian* $M_{\gamma-norm}L$ ridge strength measure for a gaussian ridge profile (equation (46) in [7]).

In the noise only scenario, $(\Theta_\sigma n) = |n''_\sigma|$. Since n''_σ is a zero-mean WSS gaussian random process with variance ν_2^2, the PDF of Θ_σ is the half-normal distribution

$$f_{\Theta_\sigma}(\theta) = \sqrt{\frac{2}{\pi}}\frac{1}{\nu_2}exp\left(-\frac{\theta^2}{2\nu_2^2}\right),\ \theta > 0. \tag{39}$$

Hence,

$$\begin{aligned} Pr\left\{(\Theta_\sigma n) > \tau\right\} &= 1 - Pr\{(\Theta_\sigma n) \leq \tau\} \\ &= 1 - \int_0^{\tau}\sqrt{\frac{2}{\pi}}\frac{1}{\nu_2}exp\left(-\frac{\theta^2}{2\nu_2^2}\right)\mathrm{d}\theta \\ &= 1 - erf\left(\frac{\tau}{\sqrt{2}\nu_2}\right), \end{aligned} \tag{40}$$

which is the probability of false impulse detection when the operator Θ_σ is applied to a signal comprising of only a zero-mean WSS gaussian random process. Then, the probability of false impulse detection in the noise only scenario by the scale-normalized smoothed second derivative operator is

$$Pr\left\{(\Theta_{\sigma,norm}n) > \tau\right\} = 1 - erf\left(\frac{\tau}{\sqrt{2}\nu_2\sigma^{1.5}}\right). \tag{41}$$

Note that the probabilities in (36) and (41) have well-behaved integrals that can be easily evaluated numerically using packages such as the Matlab (MathWorks, Natick, MA) library.

B. True Impulse Detection in the Presence of Noise

We now study the detection power of the new index by finding the probability of detecting a noise corrupted impulse signal (situated, without loss of generality at the origin) when the scale-normalized smoothed singularity index (5) (with $\gamma = 1$) is applied. Let $f(t)$ be the noise corrupted impulse signal: $f(t) = s(t) + n(t)$, where $s(t)$ is the deterministic signal and $n(t)$ is a zero-mean WSS gaussian random noise process as before. We assume $s(t)$ to be a gaussian smoothed impulse of height K and scale w as before, i.e., $s(t) = K\delta_w(t)$. Let $s_\sigma(t) = s(t) * g_\sigma(t)$, $s'_\sigma(t) = (s(t) * g_\sigma(t))'$, and $s''_\sigma(t) = (s(t) * g_\sigma(t))''$. Then the response of the scale normalized smoothed singularity index (5) applied to the noise corrupted impulse signal $f(t) = s(t)+n(t)$ may be expressed

$$\begin{aligned} (\psi_{\sigma,norm}f)(t) &= \sigma^2\frac{\left|(s_\sigma(t)+n_\sigma(t))\,(s_\sigma(t)+n_\sigma(t))''\right|}{1+\left[(s_\sigma(t)+n_\sigma(t))'\right]^2} \\ &= \frac{\left|\sigma^2\,(s_\sigma(t)+n_\sigma(t))\,(s''_\sigma(t)+n''_\sigma(t))\right|}{1+\left[(s'_\sigma(t)+n'_\sigma(t))\right]^2}. \end{aligned} \tag{42}$$

Since $s(t)$ is a deterministic signal and $n_\sigma(t)$, $n'_\sigma(t)$, and $n''_\sigma(t)$ are all zero-mean gaussian random processes, we have: $E[s_\sigma(t) + n_\sigma(t)] = s_\sigma(t)$, $var[s_\sigma(t) + n_\sigma(t)] = var[n_\sigma(t)] = \nu_0^2$, $E[s'_\sigma(t) + n'_\sigma(t)] = s'_\sigma(t)$, $var[s'_\sigma(t) + n'_\sigma(t)] = var[n'_\sigma(t)] = \nu_1^2$, $E[s''_\sigma(t) + n''_\sigma(t)] = s''_\sigma(t)$, and $var[s''_\sigma(t) + n''_\sigma(t)] = var[n''_\sigma(t)] = \nu_2^2$. Further, $s_\sigma(t)$, $s'_\sigma(t)$, and $s''_\sigma(t)$ are given by: $s_\sigma(t) =$

$\frac{Kw}{\sqrt{\sigma^2+w^2}} e^{\frac{-t^2}{2(\sigma^2+w^2)}}$, $s'_\sigma(t) = \frac{-Kwt}{(\sigma^2+w^2)^{3/2}} e^{\frac{-t^2}{2(\sigma^2+w^2)}}$, and $s''_\sigma(t) = \frac{Kw}{(\sigma^2+w^2)^{3/2}} \left(\left(\frac{t^2}{\sigma^2+w^2} - 1 \right) e^{\frac{-t^2}{2(\sigma^2+w^2)}} \right)$. At $t = 0$,

$$s_\sigma(0) = \frac{Kw}{\sqrt{\sigma^2 + w^2}},\ s'_\sigma(0) = 0,\ s''_\sigma(0) = \frac{-Kw}{(\sigma^2 + w^2)^{\frac{3}{2}}}. \quad (43)$$

Denote the random variable $(\psi_{\sigma,norm} f)(0)$ by the ratio $X_{norm}/Y = \sigma^2 X/Y$, where again X and Y are statistically independent. The random variables $(s'_\sigma(0) + n'_\sigma(0))$ is zero-mean gaussian with variance ν_1^2, since $s'_\sigma(0) = 0$. Hence, the PDF of the variable $Y = 1 + [(s'_\sigma(0) + n'_\sigma(0))]^2$ is as defined in (24).

Further, $(s_\sigma(0) + n_\sigma(0))$ and $(s''_\sigma(0) + n''_\sigma(0))$ are non-zero-mean, correlated gaussian random variables having means $s_\sigma(0)$ and $s''_\sigma(0)$, variances ν_0^2 and ν_2^2, respectively, and correlation coefficient $\rho = \frac{-\nu_1^2}{\nu_0 \nu_2}$. Unlike the zero-mean case, there exists no simple closed form expression for the PDF of the product $(s_\sigma(0) + n_\sigma(0))(s''_\sigma(0) + n''_\sigma(0))$.

Instead, let $X_1 = |(s_\sigma(0) + n_\sigma(0))|$ and $X_2 = |(s''_\sigma(0) + n''_\sigma(0))|$. Hence, the random variable $X = X_1 X_2$ is the product of two non-zero mean folded normal random processes with means $s_\sigma(0)$ and $s''_\sigma(0)$, variances ν_0^2 and ν_2^2, respectively, and correlation coefficient ρ. The PDF of the product $X = X_1 X_2$ can be determined as follows [17]:

$$f_X(x) = \int_0^\infty \frac{1}{|u|} f_{X_1 X_2}\left(u, \frac{x}{u}\right) \mathrm{d}u,\ x > 0, \quad (44)$$

where the joint PDF $f_{X_1 X_2}$ is the bivariate folded normal density function defined in (3.1) in [21]. Hence, the PDF of the numerator X_{norm} is

$$f_{X_{norm}}(x) = \frac{1}{\sigma^2} f_X\left(\frac{x}{\sigma^2}\right),\ x > 0. \quad (45)$$

Given a threshold $\tau > 0$, the probability of detecting an impulse at the origin is

$$Pr\{(\psi_{\sigma,norm} f)(0) > \tau\} = \int_{x=\tau}^\infty erf\left(\sqrt{\frac{1}{2\nu_1^2}\left(\frac{x}{\tau} - 1\right)}\right) \times f_{X_{norm}}(x)\, \mathrm{d}x, \quad (46)$$

which is arrived at by following the sequence of steps from (29) to (33).

Finally, for comparison, the probability of detecting an impulse at the origin using the scale-normalized smoothed second derivative operator $(\Theta_{\sigma,norm} f)(0) = \sigma^{1.5}(\Theta_\sigma f)(0)$ is

$$Pr\{(\Theta_{\sigma,norm} f)(0) > \tau\} = 1 - \int_0^\tau f_{\Theta_{\sigma,norm}}(\theta)\, \mathrm{d}\theta, \quad (47)$$

where

$$f_{\Theta_{\sigma,norm}}(\theta) = \frac{1}{\sqrt{2\pi}\nu_2 \sigma^{1.5}} \cdot \left[e^{-\frac{\left(\frac{\theta}{\sigma^{1.5}} - s''_\sigma(0)\right)^2}{2\nu_2^2}} + e^{-\frac{\left(\frac{\theta}{\sigma^{1.5}} + s''_\sigma(0)\right)^2}{2\nu_2^2}} \right],\ \theta > 0. \quad (48)$$

The probabilities given by (46) and (47) can again be easily evaluated numerically.

C. Simulations

The detection power and the false alarm rates of the scale-normalized singularity index and the second derivative operator were assessed using receiver operating characteristic (ROC) curves. Our simulations assumed gaussian smoothed impulses $s(t) = K\delta_w(t)$, of three different heights K (5, 10, and 20), each submerged in white gaussian noise of four different variances q^2 (5, 10, 50, and 100). The scale w of each impulse was fixed at 1.5. The scale σ of the gaussian low pass filter was set to match the impulse scale i.e., $\sigma = w = 1.5$, since we are using the scale-normalized versions of the index and the second derivative operator. We next describe the threshold selection mechanism that was used to generate the ROC curves.

For the scale-normalized smoothed singularity index, the scale-space peak response (at the origin) to a gaussian smoothed impulse in the absence of noise is scale invariant and is given by $(\psi_{\sigma=w,norm} s)(0) = \frac{K^2}{4}$ [1]. The threshold τ was varied in equal increments (set to $0.05 \times \frac{K^2}{4}$) from 0.05 to $M \times \frac{K^2}{4}$, where M is an integer that was set to 6 to yield a sufficiently large range of thresholds. Note that the range of thresholds is different for different values of K. The same thresholds were used for computing both the false alarm and true impulse detection probabilities of the scale-normalized smoothed singularity index using (36) and (46), respectively. The false alarm and true impulse detection probabilities were then subsequently used to generate the ROC curves.

Similarly, for the scale-normalized smoothed second derivative operator, the scale-space peak response to a gaussian smoothed impulse in the absence of noise is given by $(\Theta_{\sigma=w,norm} s)(0) = \frac{K}{2^{3/2}\sqrt{w}}$ [1], which is not scale invariant. Here again, the threshold τ was varied in equal increments (set to $0.05 \times \frac{K}{2^{3/2}\sqrt{w}}$) from 0.05 to $M \times \frac{K}{2^{3/2}\sqrt{w}}$, where $M = 6$. The false alarm and true impulse detection probabilities of the scale-normalized second derivative operator were computed for the same thresholds using (41) and (47), respectively, which were then used to generate the ROC curves.

Fig. 2 plots the ROC curves for the scale-normalized smoothed singularity index and the second derivative operator that were obtained using the threshold selection mechanism described above for gaussian smoothed impulses of heights $K = 5$, 10, and 20, scale $w = 1.5$, and each submerged in noise of variances $q^2 = 5$, 10, 50, and 100. The superior performance of the singularity index over the second derivative operator is immediately apparent from Fig. 2. At low noise variances (e.g., as depicted in the plot for $q^2 = 5$ in Fig. 2), the difference in ROC curves is larger for smaller values of K (e.g., $K = 5$). This accords with intuition, since one would expect that as K increases in the presence of noise having low variance, the detection power of the singularity index and the second-derivative operator would be similar. On the other hand, as the noise variance increases, the difference in ROC curves between the scale-normalized smoothed singularity index and the second derivative operator increases with K (e.g., as depicted in the plot for $q^2 = 100$ in Fig. 2). The ability of both the singularity index and the second derivative operator to reliably detect small

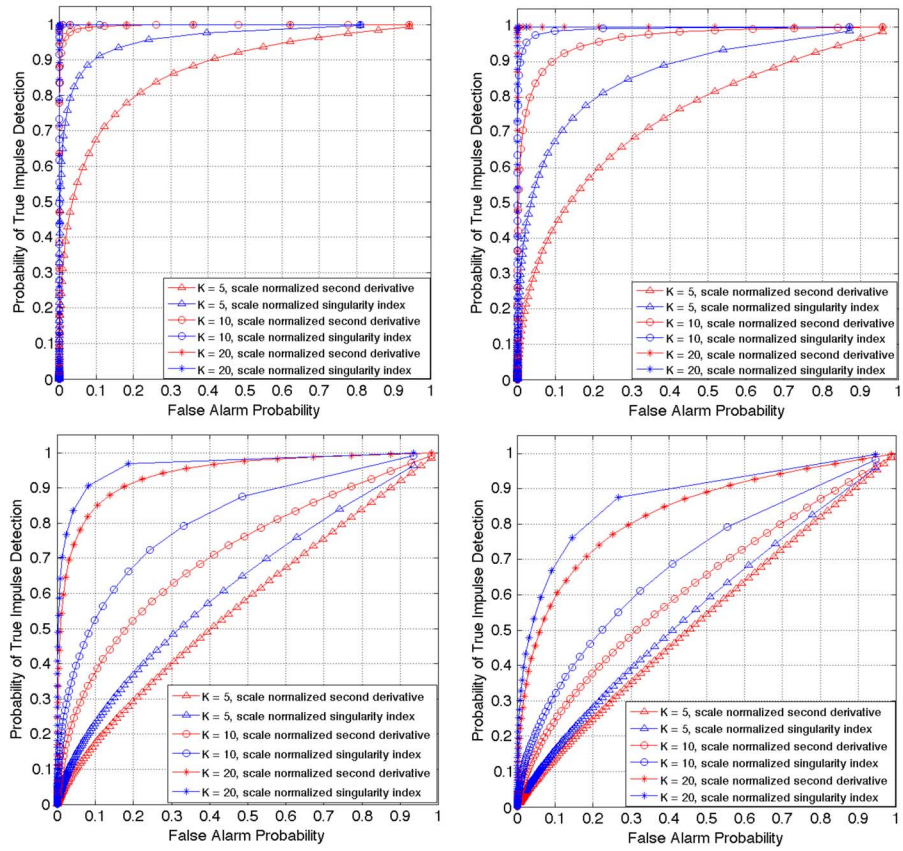

Fig. 2. ROC curves plotting the probability of true impulse detection for gaussian smoothed impulses of different heights against the false alarm probability for the scale-normalized singularity index (blue) and the second derivative operator (red). Top row: $q^2 = 5$ (left) and $q^2 = 10$ (right). Bottom row: $q^2 = 50$ (left) and $q^2 = 100$ (right). The scale w of the impulses and the scale σ of the smoothing gaussian were both fixed at 1.5.

impulses (e.g., $K = 5$) while at the same time keeping the false alarm rates low diminishes in the presence of noise having large variance. Yet, the singularity index outperforms the second derivative operator even for small impulses submerged in noise of large variance.

We also considered gaussian smoothed impulses whose scales w were different, but had the same height. Three values of w (1.5, 3, and 4.5) were considered, while K and q^2 were fixed at 10 and 100, respectively. The scale σ of the gaussian low pass filter was set to match the impulse scale w. Fig. 3 plots the ROC curves for the scale-normalized smoothed singularity index and the second derivative operator using the same threshold selection mechanism as before for the gaussian smoothed impulses of different scales. Again, the singularity index offers superior performance when compared to the second-derivative operator. What is revealing is that both the operators offer better detection power at lower false alarm rates when the scale w of the impulse increases. This is due to the fact that since the scale σ of the gaussian low pass filter is set to match the impulse scale w, the increase in σ reduces the effect of noise and yields better ROC curves. Note that as described earlier, in the absence of noise, the scale-space peak response to a gaussian smoothed impulse of scale-normalized singularity index is scale invariant. However, this does not hold when the impulse is submerged in noise.

To ascertain the veracity of the mathematical analysis used in the derivation of the detection power and the false alarm rates

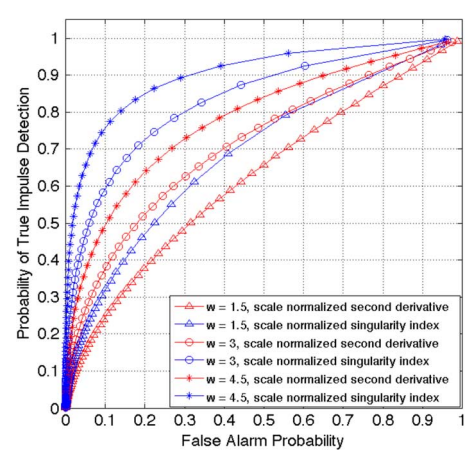

Fig. 3. ROC curves plotting the probability of true impulse detection for gaussian smoothed impulses of different scales w against the false alarm probability for the scale-normalized singularity index (blue) and the second derivative operator (red). The plots were generated for $K = 10$, $q^2 = 100$ and $\sigma = w$.

of the scale-normalized singularity index, we also plotted the empirical ROC curves along with the analytic ROC curves for the scale-normalized singularity index in Fig. 4. The following procedure was used to generate the empirical ROC curves: we considered 10000 different AWGN realizations with a notional origin and computed the index response at the origin. The false alarm rate was defined as follows: out of 10000 realizations, how many times did the index response at the origin exceed a

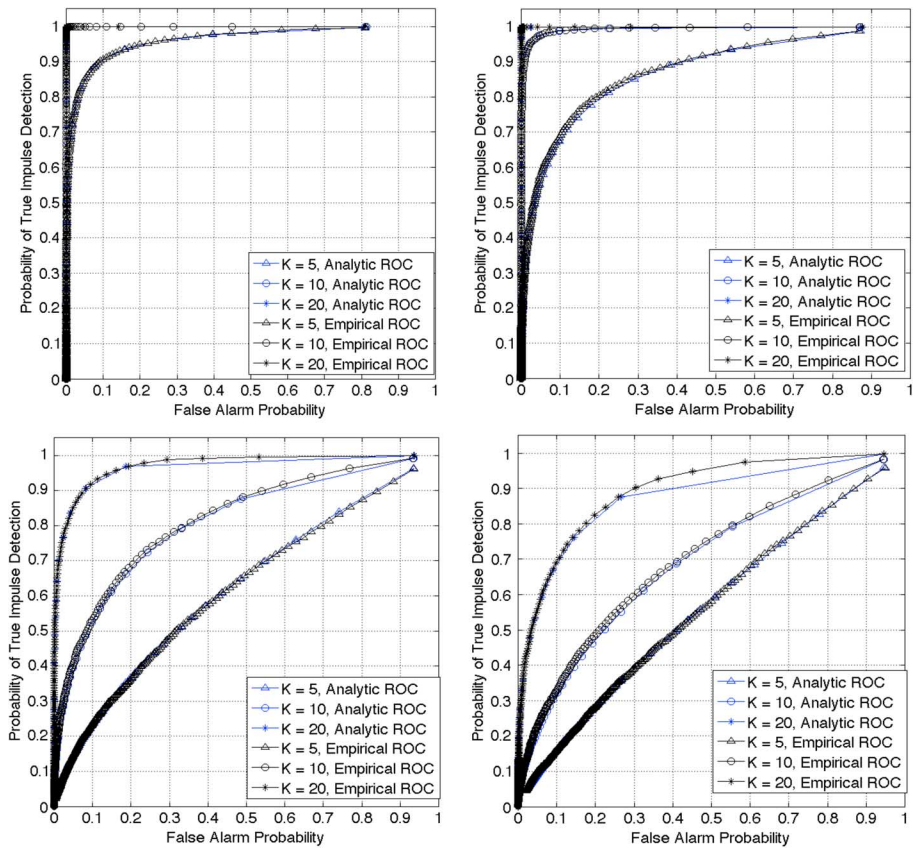

Fig. 4. Analytic (blue) and empirical (black) ROC curves plotting the probability of true impulse detection for gaussian smoothed impulses of different heights against the false alarm probability for the scale-normalized singularity index. Top row: $q^2 = 5$ (left) and $q^2 = 10$ (right). Bottom row: $q^2 = 50$ (left) and $q^2 = 100$ (right). The scale w of the impulses and the scale σ of the smoothing gaussian were both fixed at 1.5.

given threshold when applied to the noise only signal. A similar definition was used for the detection power for the signal+noise scenario. The empirical ROC curves were generated using the threshold selection mechanism described above for gaussian smoothed impulses of heights $K = 5$, 10, and 20, scale $w = 1.5$, and each submerged in noise of variances $q^2 = 5$, 10, 50, and 100. As can be seen in Fig. 4, the empirical ROC curves match the analytic ROC curves quite closely, thereby validating the mathematical analysis.

IV. Edge Suppression in the Presence of Noise

The smoothed singularity index is designed to be edge suppressing. Hence, we consider the problem of finding the probability of incorrectly detecting a noise corrupted edge at the origin when the scale-normalized smoothed singularity index defined in (5) ($\gamma = 1$) is applied. As in the impulse detection scenario, let $f(t) = s(t) + n(t)$. We model the edge signal $s(t)$ as a Heaviside step $u(t)$ of height $K > 0$ smoothed by a gaussian $g_w(t)$: $s(t) = K\Phi\left(\frac{t}{w}\right) - \frac{K}{2}$, where $\Phi\left(\frac{t}{w}\right) = \frac{1}{\sqrt{2\pi}}\int_{-\infty}^{\frac{t}{w}} e^{\frac{-x^2}{2}}\,dx$. The constant $\frac{K}{2}$ is subtracted to ensure that the edge height is 0 at the origin and symmetric about it. Then, $s_\sigma(t)$, $s'_\sigma(t)$, and $s''_\sigma(t)$ are given by: $s_\sigma(t) = K\Phi\left(\frac{t}{\sqrt{\sigma^2+w^2}}\right) - \frac{K}{2}$, $s'_\sigma(t) = \frac{K}{\sqrt{2\pi(\sigma^2+w^2)}}e^{-\frac{-t^2}{2(\sigma^2+w^2)}}$, and $s''_\sigma(t) = \frac{-Kt}{\sqrt{2\pi}(\sigma^2+w^2)^{3/2}}e^{-\frac{-t^2}{2(\sigma^2+w^2)}}$. At $t = 0$,

$$s_\sigma(0) = 0,\ s'_\sigma(0) = \frac{K}{\sqrt{2\pi(\sigma^2+w^2)}},\ s''_\sigma(t) = 0. \tag{49}$$

Again, denote the random variable $(\psi_{\sigma,norm}f)(0)$ as the ratio $X_{norm}/Y = \sigma^2 X/Y$, where X and Y are statistically independent. The PDF of X_{norm} is then

$$f_{X_{norm}}(x) = \frac{1}{\pi\sqrt{\nu_0^2\nu_2^2 - \nu_1^4}\sigma^2}K_0\left(\frac{\left|\frac{x}{\sigma^2}\right|\nu_0\nu_2}{\nu_0^2\nu_2^2 - \nu_1^4}\right) \cdot\left\{exp\left(\frac{\frac{-x}{\sigma^2}\nu_1^2}{\nu_0^2\nu_2^2 - \nu_1^4}\right) + exp\left(\frac{\frac{x}{\sigma^2}\nu_1^2}{\nu_0^2\nu_2^2 - \nu_1^4}\right)\right\},\ x > 0, \tag{50}$$

since X_{norm} is the absolute value of the product of two correlated, zero-mean gaussian random processes. The PDF of the random variable Y is

$$f_Y(y) = P(y-1),\ y > 1, \tag{51}$$

where

$$P(y) = \frac{1}{2\sqrt{2\pi(y)}\nu_1}\left[e^{-\frac{(\sqrt{y}-s'_\sigma(0))^2}{2\nu_1^2}} + e^{-\frac{(\sqrt{y}+s'_\sigma(0))^2}{2\nu_1^2}}\right]. \tag{52}$$

Then, given a threshold $\tau > 0$, the probability of detecting an edge at the origin is

$$Pr\left\{(\psi_{\sigma,norm}f)(0) > \tau\right\} = \int_{x=\tau}^{\infty}\left(\int_{z=0}^{\frac{x}{\tau}-1} P(z)\,\mathrm{d}z\right) \times f_{X_{norm}}(x)\,\mathrm{d}x. \tag{53}$$

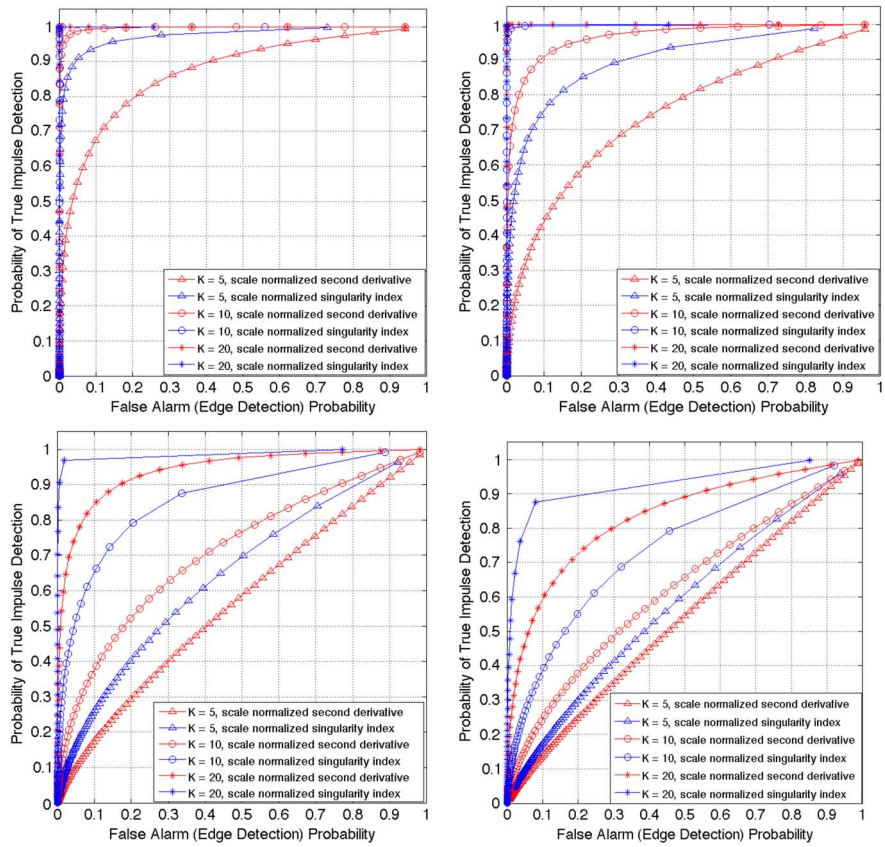

Fig. 5. ROC curves plotting the probability of true impulse detection for gaussian smoothed impulses of different heights against the false alarm probability arising out of edge detection for the scale-normalized singularity index (blue) and the second derivative operator (red). Top row: $q^2 = 5$ (left) and $q^2 = 10$ (right). Bottom row: $q^2 = 50$ (left) and $q^2 = 100$ (right). The scale w of the impulses and the scale σ of the smoothing gaussian were both fixed at 1.5.

Finally, the probability of detecting an edge at the origin by the scale-normalized second derivative operator is

$$Pr\left\{(\Theta_{\sigma,norm} f)(0) > \tau\right\} = 1 - erf\left(\frac{\tau}{\sqrt{2}\nu_2\sigma^{1.5}}\right), \quad (54)$$

which is independent of the edge height K and scale w. This follows since the random process $(s''_\sigma(0) + n''_\sigma(0))$ is zero-mean gaussian with variance ν_2^2. In fact, for the second derivative operator, the probability of detecting an edge is identical to the probability of finding an impulse (41) in the noise-only scenario!

A. Simulations

Since both the singularity index and the second derivative operator are, by design, edge suppressing, we treat the detection of an edge in the presence of noise as being identical to the false alarm scenario, i.e, detection of an impulse singularity when none is present. Hence, we plot ROC curves using the same threshold selection mechanism described in the previous section. Here again, we consider gaussian smoothed impulses of three different heights K (5, 10, and 20), each submerged in white gaussian noise of four different variances q^2 (5, 10, 50, and 100). The scale w of each impulse was fixed at 1.5 and the scale σ of the gaussian low pass filter was set to match the impulse scale.

Fig. 5 plots the ROC curves for the scale-normalized smoothed singularity index and the second derivative operator

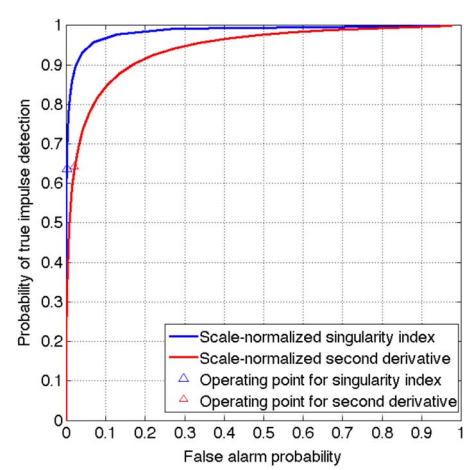

Fig. 6. Receiver operating characteristic curves for the scale-normalized 1-D singularity index (blue) and the second derivative operator (red) computed for an impulse of height $K = 20$ and scale $w = 3$ submerged in noise of variance $q^2 = 100$. The scale σ of the smoothing gaussian was also set to 3. The triangles denote the operating points on each curve corresponding to the chosen threshold values.

for gaussian smoothed impulses of heights $K = 5$, 10, and 20, scale $w = 1.5$, and each submerged in noise of variances $q^2 = 5$, 10, 50, and 100. Notice in Fig. 5 that as expected, the ROC curves for the scale-normalized second derivative operator are identical to the ROC curves plotted in Fig. 2. It is evident from Fig. 5 that the singularity index clearly outperforms the second derivative operator across the four different

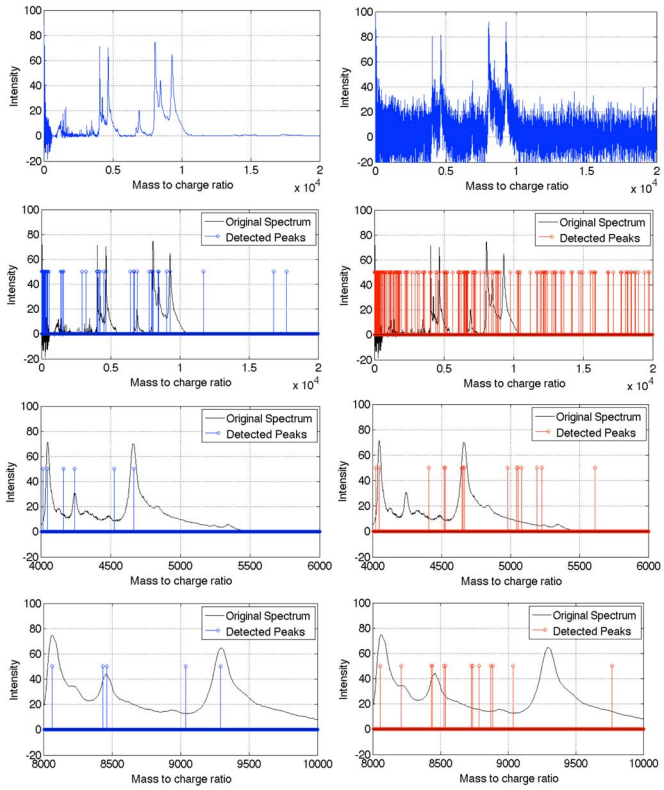

Fig. 7. Peak detection in 1-D mass spectra. Row 1: left—original spectra (normal case), right—noisy spectra generated using additive zero mean white gaussian noise of variance 100; Row 2: detected peaks; left—thresholded NMS scale-normalized singularity index response computed from the noisy spectra; right—thresholded NMS scale-normalized second derivative operator response computed from the noisy spectra; Rows 3 and 4: close-up regions showing detected peaks; left—singularity index, right—second derivative operator.

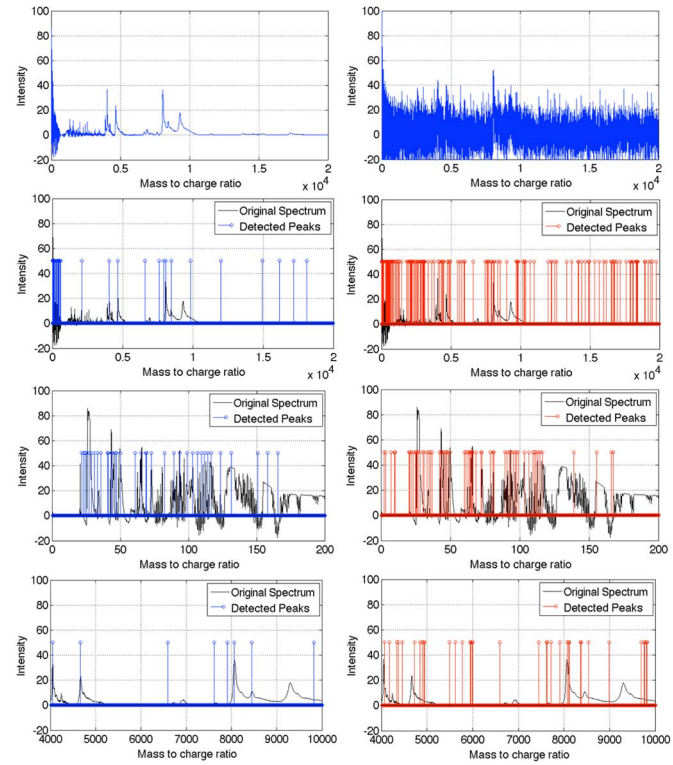

Fig. 8. Peak detection in 1-D mass spectra. Row 1: left—original spectra (ovarian cancer case), right—noisy spectra generated using additive zero mean white gaussian noise of variance 100; Row 2: detected peaks; left—thresholded NMS scale-normalized singularity index response computed from the noisy spectra; right—thresholded NMS scale-normalized second derivative operator response computed from the noisy spectra; Rows 3 and 4: close-up regions showing detected peaks; left—singularity index, right—second derivative operator.

noise variances in detecting true impulses while maintaining low false alarm rates arising out of edge detection.

V. 1-D Example Application

We demonstrate the results of the ROC analyses on two exemplar 1-D spectra (Figs. 7 and 8; row 1) from an ovarian cancer serum data set comprising both cancer and normal cases. These spectra were generated using low resolution time of flight (TOF) mass spectrometry from surface-enhanced laser/desorption ionization (SELDI) ProteinChip arrays [3]. The entire dataset can be downloaded from http://home.ccr.cancer.gov/ncifdaproteomics/ppatterns.asp (under Low Resolution SELDI-TOF Datasets, 2.1). We generated noisy spectra (Figs. 7 and 8; row 1, right column) by adding independent, zero mean white gaussian noise of variance 100 to the original spectra. It is important to note that in addition to mass spectrometry, there are many biomedical applications in which spectral measurements are used for disease detection and diagnosis (e.g., polarized reflectance spectroscopy for oral cancer detection [22] and Raman spectroscopy for skin cancer detection [23]) and these spectral measurements are often afflicted with noise that is correlated, non-white and non-gaussian. Here, we used an independent, zero mean additive white gaussian noise model to generate the noisy mass spectra to illustrate the ROC analyses.

To determine the threshold values, we used the 1-D gaussian smoothed impulse model of height $K = 20$ and scale $w = 3$ submerged in a zero-mean WSS gaussian random noise process of variance $q^2 = 100$. The scale σ of the smoothing gaussian was set equal to w. We generated ROC curves for the 1-D scale normalized singularity index and the second derivative operators by plotting the probabilities of true impulse detection against the false alarm probabilities using the threshold selection mechanism described before.

The two ROC curves are illustrated in Fig. 6. Clearly, the performance of the scale-normalized singularity index is superior to the performance of the second derivative operator on evidence of the ROC curves. On each ROC curve, we considered an operating point (denoted by the triangles in Fig. 6) where the probability of true impulse detection was approximately 0.65. The threshold values for the 1-D singularity index and the second derivative operator were based on these operating points and were set to 55.05 and 3.52, respectively.

Figs. 7 and 8 illustrate the results of peak detection obtained by thresholding the scale-normalized singularity index and the scale-normalized second derivative operator when applied to the noisy spectra (row 1, right column). The singularity index and the second derivative operator were computed over 5 scales, where the lowest scale σ of the smoothing gaussian was set to 3 pixels, while each subsequent coarser scale was larger than

the previous finer scale by a factor of $\sqrt{2}$. A simple 1-D non maxima suppression (NMS) operation was applied to the response of both the operators prior to thresholding. In the 1-D NMS implementation, the response at each point along the independent variable (here, the mass by charge ratio) was compared with the immediate left and right neighboring points and was suppressed if the response was not a local-maximum. The NMS responses were then thresholded to detect the peaks using threshold values 55.05 and 3.52 for the singularity index and the second derivative operator, respectively. As evident from rows 2 to 4 in Figs. 7 and 8, the scale-normalized singularity index detects most of the peaks whose amplitude exceeds 20, while at the same time results in lower numbers of false positive detections when compared to the scale-normalized second derivative operator.

VI. 2-D Singularity Index

The singularity index is readily extended to 2-D. The 2-D counterparts for (2) and (3) are [2]:

$$(\psi f)(x,y) = \frac{|f(x,y)|\left|\nabla^2 f(x,y)\right|}{1+|\nabla f(x,y)|^2}, \tag{55}$$

and

$$(\psi_\sigma f)(x,y) = \frac{|g_\sigma(x,y)*f(x,y)|\left|\nabla^2 g_\sigma(x,y)*f(x,y)\right|}{1+|\nabla g_\sigma(x,y)*f(x,y)|^2}, \tag{56}$$

where $f(x,y), R^2 \rightarrow R$ is a 2-D signal or function, the 2-D Laplacian operator $\nabla^2 f(x,y) = \left(\frac{\partial^2 f(x,y)}{\partial x^2}+\frac{\partial^2 f(x,y)}{\partial y^2}\right)$, the 2-D gradient operator $\nabla f(x,y) = \left(\frac{\partial f(x,y)}{\partial x}, \frac{\partial f(x,y)}{\partial y}\right)^T$, and $g(x,y)$ is a 2-D unit area isotropic smoothing gaussian $g(x,y) = \frac{1}{2\pi\sigma^2}e^{\frac{-(x^2+y^2)}{2\sigma^2}}$. In particular, if $f(x,y)$ represents the image brightness function, then the 2-D singularity index (56) is useful for detecting impulse masses in images.

It is often of interest to detect curvilinear masses in images, which have a dominant orientation along which the second order directional derivative attains a local extremum. Hence, as described in [1], the index (56) is modified to account for the dominant orientation

$$(\psi_\sigma f)(x,y) = \frac{|f_{0,\theta_D,\sigma}(x,y)f_{2,\theta_D,\sigma}(x,y)|}{1+|f_{1,\theta_D,a\sigma}(x,y)|^2}, \tag{57}$$

where $f_{0,\theta_D,\sigma}(x,y)$, $f_{1,\theta_D,a\sigma}(x,y)$, and $f_{2,\theta_D,\sigma}(x,y)$ are the responses to the zero, first and second order isotropic gaussian derivative filters along the direction specified by $\theta_D(x,y)$ and at scale σ. Estimation of $\theta_D(x,y)$ (the direction along which the second order derivative attains a local extremum) is straightforward and is achieved by exploiting the steerable property of isotropic gaussian directional derivatives as described in [24].

The first derivative response in (57) is computed at a scale $a\sigma$, where the constant $a > 0$. The constant a serves to attenuate the edge side-lobe responses produced by the index without affecting the peak response to an impulse at the origin. Following the detailed arguments made in [1], the value of a is set to 1.7754. This ensures that the peak edge side-lobe response is upper bounded by about 3.7, independent of the edge magnitude.

The scale-normalized 2-D singularity index is

$$(\psi_{\sigma,norm} f)(x,y) = \sigma^2(\psi_\sigma f)(x,y), \tag{58}$$

where σ is the scale of the isotropic smoothing gaussian. The scale-normalized 2-D index (58) can detect curvilinear masses at multiple scales. This is achieved by varying the scale σ of the isotropic smoothing gaussian and computing the maximum scale-normalized index response across all scales. Once the maximum response is computed at every location (x,y), non-maxima suppression (NMS) is applied along the dominant orientation $\theta_D(x,y)$. This design is similar to Canny's for directional edge detection [5].

We used the results of the 1-D analyses to guide the choice of threshold values for the 2-D scale-normalized singularity index $(\psi_{\sigma,norm} f)(x,y)$ and the second derivative operator responses $\sigma^{1.5}|f_{2,\theta_D,\sigma}(x,y)|$ computed on noisy images. The rationale behind using the 1-D analyses directly in the 2-D scenario is as follows: model a smoothed 2-D line impulse profile by a 2-D isotropic gaussian of strength $K > 0$ and scale σ convolved with the impulse sheet $\delta(x)$: $f(x,y) = \frac{K}{\sqrt{2\pi}\sigma}e^{\frac{-(x^2+y^2)}{2\sigma^2}} * \delta(x) = Ke^{\frac{-x^2}{2\sigma^2}}, \forall y$. Then, the conclusions regarding the response of the 2-D singularity index (55) to the 2-D line impulse profile are the same as that of the 1-D singularity index (2) for the 1-D impulse profile. Note that the analysis of the detection power and the false alarm rates of the 2-D singularity index applied to a 2-D white gaussian noise process is possible, though tedious.

The threshold values for the 2-D singularity index and the second derivative operator were based on the operating points on the two ROC curves shown in Fig. 6. Figs. 9 and 10 show examples of pristine and noisy images (rows 1 and 2, respectively). The noisy images were generated by contaminating the pristine images with independent, zero mean additive white gaussian noise of variance 100. The 2-D scale-normalized singularity index (58) and the scale-normalized second-derivative operator $\sigma^{1.5}|f_{2,\theta,\sigma}(x,y)|$ responses (with NMS) were computed over 5 scales on the noisy images illustrated in Figs. 9 and 10. It is worth reiterating here that the scale-normalized second-derivative operator $\sigma^{1.5}|f_{2,\theta,\sigma}(x,y)|$ corresponds exactly to Lindeberg's $M_{\gamma-norm}L$ ridge strength measure defined in (46) in [7]. The lowest scale σ of the isotropic gaussian was set to 3 pixels, while each subsequent coarser scale was larger than the previous finer scale by a factor of $\sqrt{2}$. The NMS responses were then thresholded to detect curvilinear masses using threshold values 55.05 and 3.52 for the singularity index and the second derivative operator, respectively.

The results of the thresholding are shown in rows 3 and 4 for the singularity index and the second derivative operator, respectively. Also, a close-up view of the results is shown in Fig. 11. It is evident from row 3 in Figs. 9 and 10, and from row 2 in Fig. 11 that the singularity index detects most of the salient curvilinear structures with good contour continuity while at the same time suppressing edges. On the other hand, the second derivative operator results in a lot more clutter and in the detection of edges

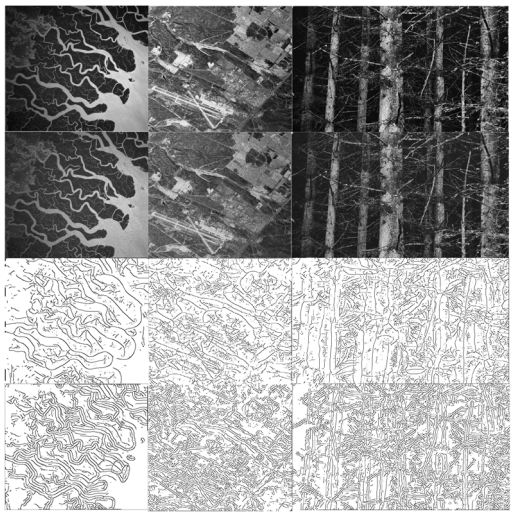

Fig. 9. Row 1: Original images (column 1: The Ganges river delta, NASA, courtesy of nasaimages.org, column 2: An aerial image (courtesy University of Southern California), column 3: An image of pine tree trunks), row 2: Corresponding noisy images (additive zero mean white gaussian noise of variance 100), row 3: Curvilinear structures detected on thresholding the NMS scale-normalized singularity index response, and row 4: Curvilinear structures detected on thresholding the NMS scale-normalized second derivative operator response.

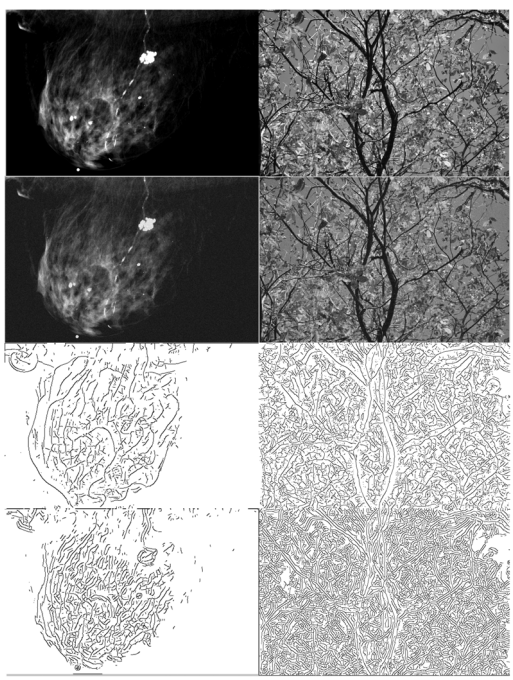

Fig. 10. Row 1: Original images (column 1: A Mammogram courtesy Emory University, Atlanta, GA, column 2: A foliage scene captured by the authors), row 2: Corresponding noisy images (additive zero mean white gaussian noise of variance 100), row 3: Curvilinear structures detected on thresholding the NMS scale-normalized singularity index response, and row 4: Curvilinear structures detected on thresholding the NMS scale-normalized second derivative operator response.

as well. The detection of edges by the second derivative operator should not be surprising, since as shown in our analyses, the probability of falsely detecting an impulse in the noise only scenario is exactly the same as the probability of detecting an edge suppressed in noise.

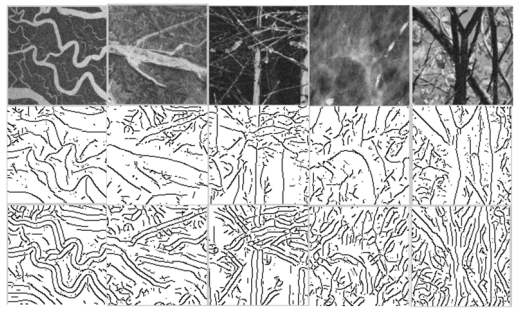

Fig. 11. A close-up view of the results. Row 1: a region of interest (ROI) from the noisy images illustrated in row 2 in Figs. 9 and 10 (column 1: from Ganges river delta, column 2: from the aerial image, column 3: from the image of the pine tree trunks, column 4: from the mammogram, and column 5: from the foliage scene) row 2: Corresponding ROI from the binary scale-normalized singularity index response, and row 3: Corresponding ROI from the binary scale-normalized second derivative operator response.

VII. 2-D Example Application

To illustrate a practical application of the new singularity index, we consider the problem of automated segmentation of vessels in 2-D color images of the retina. Segmentation of retinal vessels is an important pre-processing step in the automated screening of diabetic retinopathy. We used the publicly available DRIVE database of retina images [25]. The images in the database were acquired using a Canon CR5 non-mydriatic 3CCD camera with a 45 degree field of view (FOV). Each image in the database has an associated ground truth depicting the true vessels in the image. The details of the image acquisition and ground truth generation can be found in [25].

We compared the performance of the 2-D scale-normalized singularity index with the scale-normalized second derivative operator for extracting vessels in the retina images. As described in [25], the processing was carried out on the green channel of the RGB images at the following scales: 0.5, 1, 2, and 4 pixels. Prior to computing the index and the second derivative response, the images were locally normalized to 0 mean and unit variance using a gaussian de-biasing filter of scale $\lambda = 40$ pixels. This pre-processing is exactly as described in [25]. There were a total of 20 test images in the DRIVE database and the performance of both of the operators was evaluated using ROC analysis, which is a standard evaluation methodology for evaluating detection performance on medical imaging data [25].

Fig. 12 illustrates the ROC curves of the vessel detection performance of both the scale-normalized singularity index and the second derivative operators. The area under the curve (AUC) values were 0.8176 and 0.7494 for the scaled-normalized singularity index and the second derivative operator, respectively. The scale-normalized singularity index does a better job of automatically segmenting vessels as compared to the scale-normalized second derivative operator. Note that this experiment was completely unsupervised and no training data was used to select any parameters for the two operators. With training and the use of a classifier to classify pixels as vessel or non-vessel, one could expect even better performance using the new singularity index. Fig. 13 illustrates an example retina image, ground truth depicting the vessels, and vessels detected by the scale-normalized singularity index and the second derivative operator. The

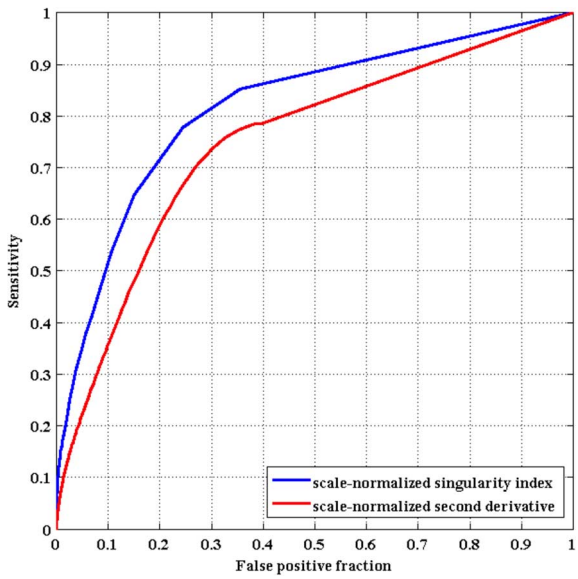

Fig. 12. ROC curves illustrating the vessel detection performance of the scale-normalized singularity index and the second derivative operator on the DRIVE retina image database.

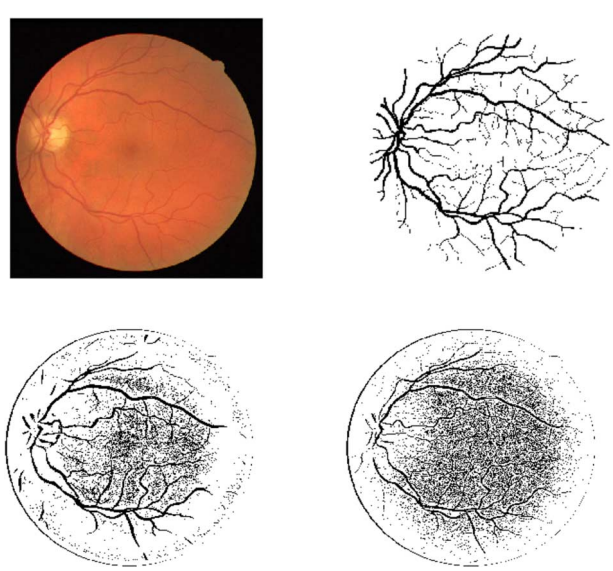

Fig. 13. Vessel detection on an example retina image. Top row: left: an example retina image from the DRIVE Database; right: ground truth vessel segmentation. Bottom row: Detected vessels. Left: scale-normalized singularity index; right: scale-normalized second derivative.

binary results were obtained by thresholding the response of the two operators at a sensitivity of 50%. It is evident from Fig. 13 that the scale-normalized singularity index produces a better segmentation of the vessels than the second derivative operator (fewer false positives at a given sensitivity).

VIII. Conclusion

This paper develops detailed theoretical analyses of the detection power and false alarm probabilities of a new 1-D singularity index that was recently designed for impulse detection in signals of arbitrary dimensionality [1], [2]. By design, the singularity index amplifies response to impulses, while at the same time delivering powerful attenuation to edges. Our theoretical analyses and subsequent simulations involving ROC curves and experiments with real 1-D signals and images corroborate this claim. By comparison, the simple second derivative operator, which is a nominal impulse detector fails in reliably detecting impulses and suppressing edges in a noisy environment. The index is naturally scalable and is computationally efficient, since it exploits the steerable property of isotropic gaussian derivatives.

Two interesting directions that we plan to pursue as part of future work include generalization of the 2-D singularity index by defining the kth-order index [1]

$$\psi_\sigma^k\left[f(x)\right] = \frac{\left|g_\sigma^{k-1} * f(x)\right| \left|g_\sigma^{k+1} * f(x)\right|}{1 + \left|g_{a\sigma}^k * f(x)\right|^2}. \tag{59}$$

Clearly (3) is a special case of (59) when $k = 1$. Further, $k = 2$ yields an edge detector. We plan to study the kth-order index (59) in detail. Of particular interest is to analyze what types of higher order singularities other than impulses and edges can be detected within the framework of the kth-order index.

Our analyses has been based on the assumption that the noise is independent and white, although by gaussian low pass filtering, the noise spectrum is modified and is no longer white. Going forward, we plan to study the detection of impulses in images corrupted by speckle noise. Analysis with speckle is challenging due to the high degree of correlation and signal dependence that typically characterizes speckle. Yet, this is important since there are many imaging applications based on coherent processing that generate images afflicted with speckle, which impacts the ability of a computer vision system to detect features of interest such as ridges and edges. Examples of such imaging applications include synthetic aperture radar [26] and optical coherence tomography [27].

References

[1] G. S. Muralidhar, A. C. Bovik, and M. K. Markey, "A steerable, multi-scale singularity index," *IEEE Signal Process. Lett.*, vol. 20, no. 1, pp. 7–10, 2013.
[2] G. S. Muralidhar, A. C. Bovik, and M. K. Markey, "A new singularity index," in *Proc. IEEE Int. Conf. Image Process.*, 2012.
[3] T. P. Conrads, V. Fusaro, S. Ross, D. Johann, V. Rajapakse, B. A. Hitt, S. M. Steinberg, E. C. Kohn, D. A. Fishman, G. Whitely, J. C. Barrett, L. A. Liotta, E. F. Petricoin, and T. D. Veenstra, "High-resolution serum proteomic features for ovarian cancer detection," *Endocr. Relat. Cancer*, vol. 11, no. 2, pp. 163–178, 2004.
[4] H. Shin, M. P. Sampat, J. M. Koomen, and M. K. Markey, "Wavelet-based adaptive denoising and baseline correction for Maldi TOF MS," *OMICS*, vol. 14, no. 3, pp. 283–295, 2010.
[5] J. Canny, "A computational approach to edge detection," *IEEE Trans. Pattern Anal. Mach. Intell.*, vol. 8, no. 6, pp. 679–698, 1986.
[6] S. Mallat and W. L. Hwang, "Singularity detection and processing with wavelets," *IEEE Trans. Inf. Theory*, vol. 38, no. 2, pp. 617–643, 1992.
[7] T. Lindeberg, "Edge detection and ridge detection with automatic scale selection," *Intl. J. Comput. Vision*, vol. 30, no. 2, pp. 117–154, 1998.
[8] T. Lindeberg, "Feature detection with automatic scale selection," *Intl. J. Comput. Vision*, vol. 30, no. 2, pp. 77–116, 1998.
[9] C. Steger, "An unbiased detector of curvilinear structures," *IEEE Trans. Pattern Anal. Mach. Intell.*, vol. 20, no. 2, pp. 113–125, 1998.
[10] T. M. Koller, G. Gerig, G. Szekely, and D. Dettwiler, "Multiscale detection of curvilinear structures in 2-d and 3-d image data," in *Proc. IEEE Int. Conf. Comput. Vision*, 1995, pp. 864–869.
[11] J. F. Kaiser, "Some useful properties of Teager's energy operators," in *Proc. IEEE Int. Conf. Acoust., Speech, Signal Process.*, 1993, vol. 3, pp. 149–152.
[12] A. C. Bovik, P. Maragos, and T. F. Quatieri, "AM-FM energy detection and separation in noise using multiband energy operators," *IEEE Trans. Signal Process.*, vol. 41, no. 12, pp. 3245–3265, 1993.

[13] D. Dimitriadis and P. Maragos, "Continuous energy demodulation methods and application to speech analysis," *Speech Commun.*, vol. 48, no. 7, pp. 819–837, 2006.
[14] I. Kokkinos, G. Evangelopoulos, and P. Maragos, "Texture analysis and segmentation using modulation features, generative models, weighted curve evolution," *IEEE Trans. Pattern Anal. Mach. Intell.*, vol. 31, no. 1, pp. 142–157, 2009.
[15] S. Mallat and S. Zhong, "Characterization of signals from multiscale edges," *IEEE Trans. Pattern Anal. Mach. Intell.*, vol. 14, no. 7, pp. 710–732, 1992.
[16] S. Zhang and M. A. Karim, "A new impulse detector for switching median filters," *IEEE Signal Process. Lett.*, vol. 9, no. 11, pp. 360–363, 2002.
[17] A. Papoulis and S. U. Pillai, *Probability, Random Variables and Stochastic Processes*, 4th ed. New York, NY, USA: McGraw-Hill, 2002.
[18] A. Cedilnik, K. Kosmelj, and A. Blejec, "Ratio of two random variables: A note on the existence of its moments," *Metodoloski zvezki*, vol. 3, no. 1, pp. 1–7, 2006.
[19] L. Isserlis, "On a formula for the product-moment coefficient of any order of a normal frequency distribution in any number of variables," *Biometrika*, vol. 12, no. 1/2, pp. 134–139, 1918.
[20] I. S. Gradshteyn and I. M. Ryzhik, *Table of Integrals, Series, Products*, 5th ed. San Diego, CA, USA: Academic, 1994.
[21] S. Psarakis and J. Panaretos, "On some bivariate extensions of the folded normal and the folded t distributions," *J. Appl. Statist. Sci.*, vol. 10, no. 2, pp. 119–136, 2001.
[22] L. T. Nieman, C. W. Kan, A. Gillenwater, M. K. Markey, and K. Sokolov, "Probing local tissue changes in the oral cavity for early detection of cancer using oblique polarized reflectance spectroscopy: A pilot clinical trial," *J. Biomed. Opt.*, vol. 13, no. 2, pp. 024 011-1–024 011-11, 2008.
[23] C. A. Lieber, S. K. Majumder, D. Billheimer, D. L. Ellis, and A. Mahadevan-Jansen, "Raman microspectroscopy for skin cancer detection *in vitro*," *J. Biomed. Opt.*, vol. 13, no. 2, pp. 024 013-1–024 013-9, 2008.
[24] W. T. Freeman and E. H. Adelson, "The design and use of steerable filters," *IEEE Trans. Pattern Anal. Mach. Intell.*, vol. 13, no. 9, pp. 891–906, 1991.
[25] J. Staal, M. Abramoff, M. Niemeijer, M. Viergever, and B. van Ginneken, "Ridge-based vessel segmentation in color images of the retina," *IEEE Trans. Med. Imag.*, vol. 23, no. 4, pp. 501–509, 2004.
[26] L. J. Porcello, N. G. Massey, R. B. Innes, and J. M. Marks, "Speckle reduction in synthetic-aperture radars," *J. Opt. Soc. Amer.*, vol. 66, no. 11, pp. 1305–1311, 1976.
[27] A. F. Fercher, W. Drexler, C. K. Hitzenberger, and T. Lasser, "Optical coherence tomography—Principles and applications," *Rep. Progr. Phys.*, vol. 66, no. 2, p. 239, 2003.

Gautam S. Muralidhar (S'10–M'12) received the B.E. degree in electronics and communications engineering from the Visveswaraya Technological University, Belgaum, India, in July 2002, and the M.S.E and the Ph.D. degrees in biomedical engineering from The University of Texas at Austin (UT-Austin), in May 2009 and December 2012, respectively.

At UT-Austin, he was a member of the Laboratory for Image and Video Engineering (LIVE) and The Biomedical Informatics Laboratory (BMIL). Prior to joining UT-Austin, he worked as a software engineer at Philips Healthcare, a division of Philips Electronics India Ltd., in Bangalore, India, from July 2003–July 2007, and as a software engineer at Oracle India Development Center, Hyderabad, India, from July 2002–July 2003.

Dr. Muralidhar was a recipient of The University of Texas Continuing Graduate Fellowship during the 2011–2012 academic year, Medical Image Perception Society's Student Scholarship in 2011, and The University of Texas Professional Development Award in 2011.

Alan C. Bovik (F'96) is the Curry/Cullen Trust Endowed Chair Professor at The University of Texas at Austin, where he is Director of the Laboratory for Image and Video Engineering (LIVE). He is a faculty member in the Department of Electrical and Computer Engineering and the Center for Perceptual Systems in the Institute for Neuroscience. His research interests include image and video processing, computational vision, and visual perception. He has published more than 650 technical articles in these areas and holds two U.S. patents. His several books include the recent companion volumes: *The Essential Guides to Image and Video Processing* (New York: Academic, 2009).

Prof. Bovik was named Honorary Member of IS&T in 2013, and received the SPIE Technology Achievement Award for 2012. He was also named the SPIE/IS&T Imaging Scientist of the Year for 2011. He has also received a number of major awards from the IEEE Signal Processing Society, including: the Best Paper Award (2009); the Education Award (2007); the Technical Achievement Award (2005), and the Meritorious Service Award (1998). He received the Hocott Award for Distinguished Engineering Research at the University of Texas at Austin, the Distinguished Alumni Award from the University of Illinois at Champaign-Urbana (2008), the IEEE Third Millennium Medal (2000) and two journal paper awards from the international Pattern Recognition Society (1988 and 1993). He is a Fellow of the Optical Society of America (OSA), a Fellow of the Society of Photo-Optical and Instrumentation Engineers (SPIE), and a Fellow of the American Institute of Medical and Biomedical Engineering (AIMBE). He has been involved in numerous professional society activities, including: Board of Governors, IEEE Signal Processing Society, 1996–1998; cofounder and Editor-in-Chief, IEEE TRANSACTIONS ON IMAGE PROCESSING, 1996–2002; Editorial Board, PROCEEDINGS OF THE IEEE, 1998–2004; Series Editor for *Image, Video, and Multimedia Processing* (New York: Morgan and Claypool, 2003–present); and Founding General Chairman, First IEEE International Conference on Image Processing, held in Austin, TX, in November 1994. He is a registered Professional Engineer in the State of Texas and is a frequent consultant to legal, industrial and academic institutions.

Mia K. Markey (SM'09) is a 1994 graduate of the Illinois Mathematics and Science Academy. She received the B.S. degree in computational biology in 1998 from Carnegie Mellon University and the Ph.D. degree in biomedical engineering in 2002, along with a certificate in bioinformatics, from Duke University.

She is an Engineering Foundation Endowed Faculty Fellow in Engineering at The University of Texas at Austin, Associate Professor of Biomedical Engineering at The University of Texas at Austin, and Adjunct Associate Professor of Imaging Physics at The University of Texas MD Anderson Cancer Center. Her lab designs decision support systems for clinical decision making and scientific discovery using artificial intelligence and signal processing technologies. Her research portfolio also includes projects in biometrics.

Dr. Markey has been recognized for excellence in research and teaching with awards from organizations such as the American Medical Informatics Association, the American Society for Engineering Education, and the American Cancer Society.